Ore Geology Reviews 82 (2017) 170–180

Contents lists available at ScienceDirect

Ore Geology Reviews

journal homepage: www.elsevier.com/locate/oregeo

Primary diagenetic copper carbonate at the Malbunka copper deposit, Amadeus Basin, Northern Territory, Australia

Erik B. Melchiorre [a,b,*], Dehne McLaughlin [c], Ralph Bottrill [d], Jay Hight [a]

[a] Department of Geology, California State University, 5500 University Parkway, San Bernardino, CA 92407, USA
[b] Department of Earth Sciences, University of California Riverside, 900 University Avenue, Riverside, CA 92521, USA
[c] Malbunka Copper Mine, 5 Tenth Avenue, West Moonah, Tasmania 7009, Australia
[d] Mineral Resources Tasmania, PO Box 56, Rosny Park, Tasmania 7018, Australia

ARTICLE INFO

Article history:
Received 17 August 2016
Received in revised form 5 November 2016
Accepted 8 November 2016
Available online 7 December 2016

Keywords:
Azurite
Malachite
Carbon isotope
Thermometry
Diagenesis

ABSTRACT

The Malbunka copper deposit, located about 220 km west of Alice Springs, in the Northern Territory of Australia, may be a rare example of primary formation of copper carbonate mineralization. This deposit consists of unusual azurite disks up to 25 cm diameter, and lesser amounts of secondary azurite crystals and malachite. Carbon isotope values of the copper carbonate minerals are consistent with formation from groundwater-dissolved inorganic carbon. Oxygen isotope thermometry formation temperature estimates are 5–16 °C above ambient temperatures, suggesting the copper carbonates formed at a depth between 0.3 and 1.6 km in the Amadeus Basin. Azurite fluid inclusion waters are rich in boron, chlorine, and other elements suggestive of dilute oil basin formation fluids. In addition, presence of euhedral tourmaline with strong chemical zonation suggest that this was a low temperature diagenetic setting. The strong correlation of structures associated with hydraulic fracturing and rich copper carbonate mineralization suggest a strongly compartmentalized overpressure environment. It is proposed that copper carbonates of the Malbunka deposit formed when deep, copper-rich formation fluids were released upward by overpressure-induced failure of basin sediments, permitting mixing with carbonate-rich fluids above. This work bears directly upon exploration for a new type of primary copper deposit, through understanding of the conditions of genesis.

1. Introduction

The Malbunka Copper Mine is located on Ltalaltuma Aboriginal Trust lands, approximately 220 km west of Alice Springs, in the Northern Territory of Australia (Fig. 1). Copper mineralization was discovered at Malbunka in the 1950s by the Aboriginal artist Albert Namatjira, and was originally known as the Namatjira Prospect. The deposit was prospected in the 1960s with bulldozer cuts and a 40 m long adit driven at 5 degrees down the slope of the anticlinal axis. The deposit was deemed to be not economic at the time, because of a low grade and small tonnage. Access to the site requires a travel permit from the Central Land Council. The site became noted in the 1970s for an unusual and attractive association of blue azurite disks on a white clay matrix. These mineral specimens were first reported in print by Sullivan (1979), where he describes azurite sun specimens from the mine that were sold at shows in Europe. The mine site is operated under Northern Territory Mineral Lease 29,494 by Dehne McLaughlin, for production of mineral specimens, with the consent of the traditional Aboriginal owners. A detailed history and description of the operations is provided in McLaughlin and Grant (2012).

1.1. Deposit geology and mineralogy

The oil-bearing Amadeus Basin, of which the Arumbera Sandstone is a distinctive member, is a sequence of marine and terrestrial deltaic-fluvial sediments deposited from the late Precambrian to the Devonian (Fig. 1). The Arumbera Sandstone is the key reservoir in the Dingo and Orange gas fields (e.g., Ambrose, 2006). It was uplifted starting in the late Devonian and faulted and folded in a major compressional event between 400 and 300 Ma (Haines et al., 2001). Seismites are common in the Arumbera Sandstone and are present in the mine site sandstone bounding the kaolinite lens (Girardi, 2012; McLaughlin and Grant, 2012).

The Malbunka copper deposit occurs in the Namatjira Formation; a mixed carbonate and clastic sequence with sandstone,

* Corresponding author at: Department of Geology, California State University, 5500 University Parkway, San Bernardino, CA 92407, USA.
E-mail addresses: emelch@csusb.edu (E.B. Melchiorre), dehne.mclaughlin@bigpond.com (D. McLaughlin), ralph.bottrill@stategrowth.tas.gov.au (R. Bottrill).

http://dx.doi.org/10.1016/j.oregeorev.2016.11.021
0169-1368/

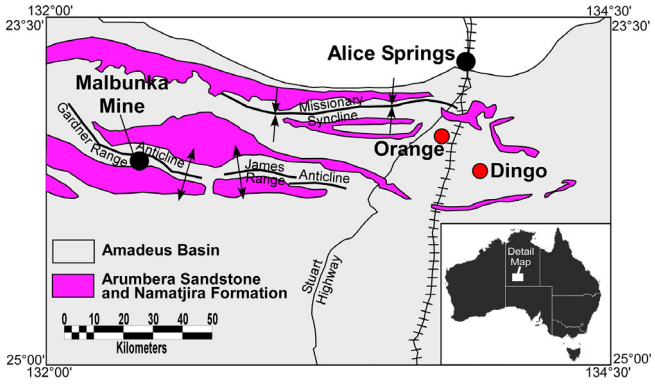

Fig. 1. Index map of the study area, showing extent of the Amadeus Basin, the Dingo and Orange gas fields, the limits of the Arumbera Sandstone and Namatjira Formation, and locations of major geological structures.

carbonate mudstone and shale. The Namatjira formation is Eocambrian in age (Lindsay, 1987; Mapstone and McIlroy, 2006), and is only known in the Gardiner Range of the Amadeus Basin. The Namatjira Formation is the lateral equivalent of the Arumbera Sandstone, as described by Warren and Shaw (1995). Edgoose (2013) advises that the Eninta Sandstone is now mapped as Arumbera Sandstone. The Arumbera Sandstone can be up to 1300 m thick and is copper-bearing over a wide area. In Ellery Creek, about 100 km from the mine, the formation hosts malachite, covellite, chalcocite, and possibly chalcopyrite and cuprite (Freeman et al., 1987). Laurie et al. (1991) also point out the affinity of copper for the Arumbera Sandstone, and postulated that these deposits formed from copper-rich basin brines. Salt diaparism and associated halotectonics in the Amadeus Basin is likely to have a base metal association and should be considered in formulating exploration strategies (Dyson and Marshall, 2005).

At the Malbunka copper deposit, disk-shaped azurite masses occur within a white to red kaolinite lens up to 2.75 m thick and bounded below and above by grey clay-rich Arumbera Sandstone (Fig. 2). The clay lens is fault-bounded with approximate lateral dimensions of 50 by 40 m and has the appearance of a channel deposit with bedding structures. This kaolinite lens occurs at the crest of the Gardiner Range Anticline and outcrops beside roadsides across the Central basin to the west and north in the West MacDonnell National Park (Cook, 1968; Fig. 1).

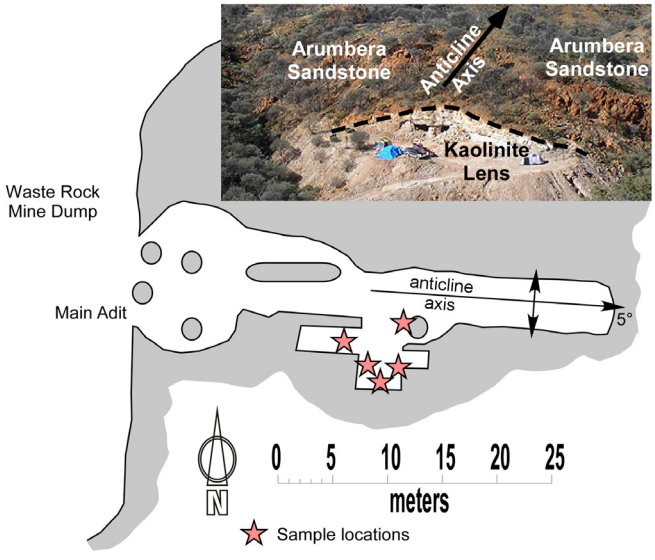

Fig. 2. Plan map of Malbunka mine workings, showing general structure and sample locations. The inset photo shows geology (blue tent and white truck for scale).

Azurite is the most common copper mineral found in the deposit. Light to deep blue disks of azurite are normally from 2.5 to 13 cm in diameter and rarely reach 25 cm in diameter (Fig. 3). These azurite specimens have a unique discoidal form, and are comprised of numerous small flat crystals of azurite arranged in radial and concentric forms (McLaughlin and Grant, 2012). They occupy bedding planes, relic thrust fault planes, and joints in the white and less commonly the red kaolinite host. The off white colour of the kaolinite in the azurite rich portions of the mineralized bed is probably due to bleaching of the clay by the mineralizing solutions (McLaughlin and Grant, 2012). Higher concentrations of iron oxide or lack of bleaching, gives the kaolinite a red colour for at least two thirds of the layer (Fig. 4). In rare cases, azurite crystal clusters (Fig. 5) and 3-dimesional rounded to oblate malachite nodules are evident in bedding planes, clefts and channels in the hanging wall, soft sediment flow planes, and fractures in the kaolinite. The azurite is at its highest concentration within 30 cm of the upper sandstone in a series of up to five thin horizontal bedding planes. In the bedding plane closest to the upper sandstone large diameter (13–25 cm) azurite specimens are found, sometimes in direct contact with the sandstone. Azurite disks, exposed in mine entrance support pillars, are also present in the kaolinite within 30 cm of the contact of the kaolinite with the lower footwall sandstone, but are not persistent throughout the footwall area of the kaolinite lens. Azurite occurs occasionally as large light blue disks in iron oxide rich kaolinite throughout the kaolinite lens.

Malachite is occasionally found in the deposit, and occurs in two forms. The first, and most common, is as disks of oblate spheroidal or ellipsoid forms which appear to be unrelated to pseudomorphous replacement of azurite (Fig. 6a). These forms rarely exhibit crystal growth structures. The second, and rarer malachite occurrence, is pseudomorphous replacement of azurite disks. These often display faithful crystal replacement (Fig. 6b). Atacamite is abundant in the upper and lower sandstone, and rims the kaolinite-sandstone contact, and occurs as disseminated fine-grained crystals. Chrysocolla is rare in the deposit, and has only been reported from the lower sandstone in association with atacamite (McLaughlin and Grant, 2012). Traces of chalcocite, covellite, digenite, and cuprite are also reported as fracture fillings and small masses. A highly fractured and copper-mineralized zone which may have served as a primary fluid conduit is exposed below the clay unit.

The unusual occurrence of azurite as flattened disks was attributed by Sullivan (1979) to azurite replacement of marine life or algae. Warren and Shaw (1995) report that the lower Arumbera Sandstone has yielded specimens of the soft-bodied Ediacarian fauna and that there is a diversity of trace fossils in the upper Arumbera Sandstone. The Ediacarian organism *Dickinsonia costata* does indeed bear a crude resemblance to the general size and shape of the azurite disks, as does *Aspidella terranovica* (Fig. 7).

2. Methods

2.1. Sample preparation and mineralogical characterization

Samples of azurite and malachite were collected and cleaned of white clay matrix. For each locality, a single disk or nodule was selected, then subdivided for analysis by different methods. Material for scanning electron microscope (SEM) and electron microprobe (probe) analysis were prepared using the standard methodology of microanalysis laboratories around the world (e.g., Goldstein et al., 2003; Reed, 2005). Samples for stable isotope

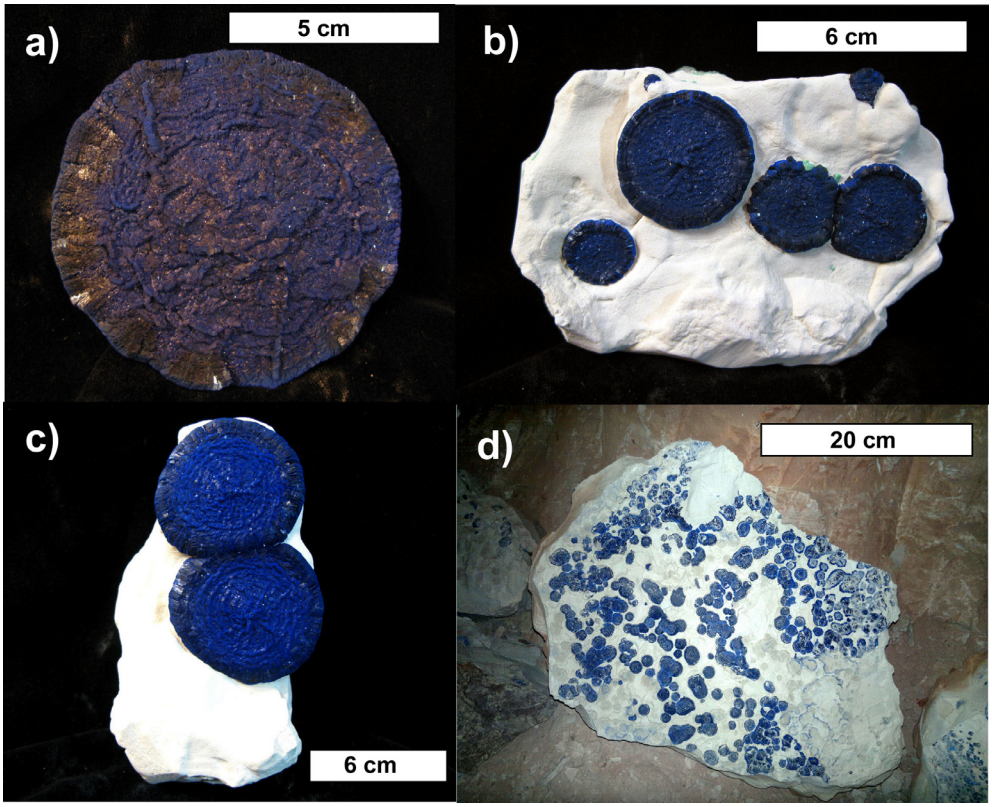

Fig. 3. Examples of azurite disks showing a) radial growth habit and detail, b) typical disk size, c) intergrowth relationships, and d) population density and distribution.

Fig. 4. Typical relationship of red and white clay types.

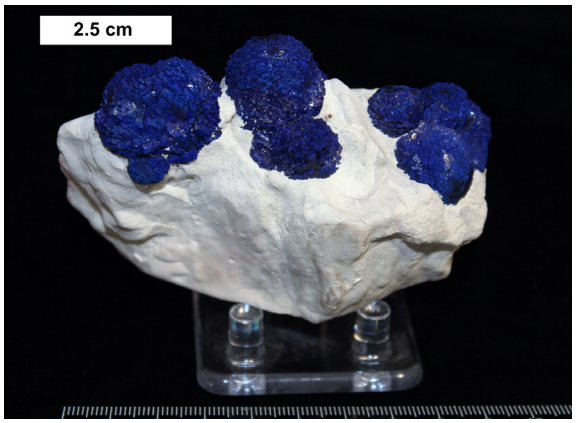

Fig. 5. Example of 3-dimensional azurite crystal habit. Specimen is 10 cm wide, with largest crystal cluster 2.5 cm diameter.

analysis were crushed in an agate mortar to pass through a 100-mesh screen (<0.147 mm). Resulting powders were scanned by X-ray diffraction (XRD) to check purity. The remainder of the sample was reserved for inclusion studies. Samples of white clay matrix were lightly crushed, washed, and panned to produce a sand-sized heavy mineral concentrate. The heavy sand fraction from the clay was studied by optical microscopy and mounted for electron microprobe chemical analysis. Clay was also examined by XRD to determine its mineralogy.

2.2. Geochemical analyses

Backscatter electron images and element analyses were generated using a CAMECA SX100 electron microprobe at the University of Arizona Lunar and Planetary Laboratory. The microprobe is equipped with five tunable wavelength dispersive spectrometers. Operating conditions were 40° takeoff angle, and beam energy of 15 keV. The beam current was 20 nA, and the beam diameter was 1 μm. Counting time was 60 s. Well-characterized natural and synthetic minerals were used for in-house standards. Detection limits were better than 0.02 wt% for all elements. Analytical sensitivity (at the 99% confidence level) ranged from 0.263% relative for Si Ka to 2.795% relative for S Ka. The matrix correction method was ZAF/Phi–Rho–Z calculations with an Armstrong/Love Scott algorithm (Armstrong, 1988).

Samples for fluid inclusion study were crushed under vacuum, with the liberated fluid collected in a liquid nitrogen trap. Samples were taken off-line in a break-seal, and analysed for fluid chemistry by ICP-MS at Babcock & Sons Laboratories of Riverside, CA, with a split reserved for stable isotope analysis.

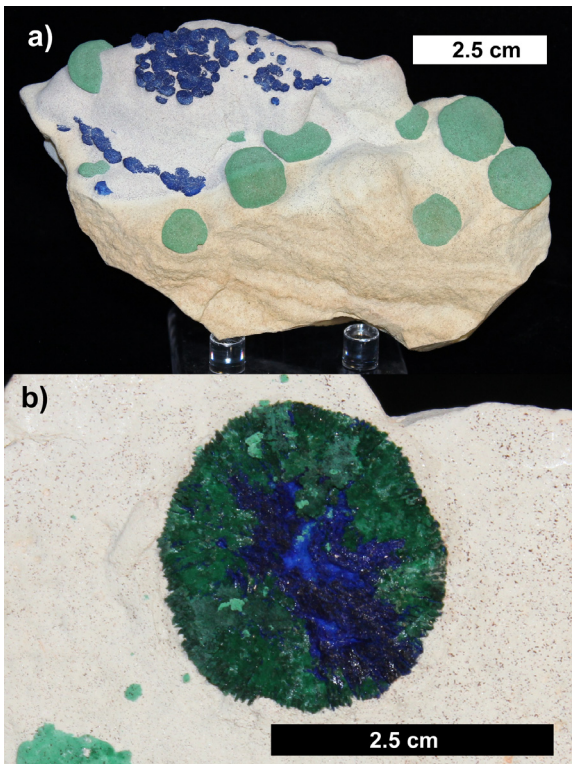

Fig. 6. Examples of a) Malachite ellipsoids in association with azurite disks. Specimen is 11.5 cm across, and largest malachite disk is 1.5 cm diameter. b) pseudomorphous replacement of a 2.5 cm azurite disk by malachite.

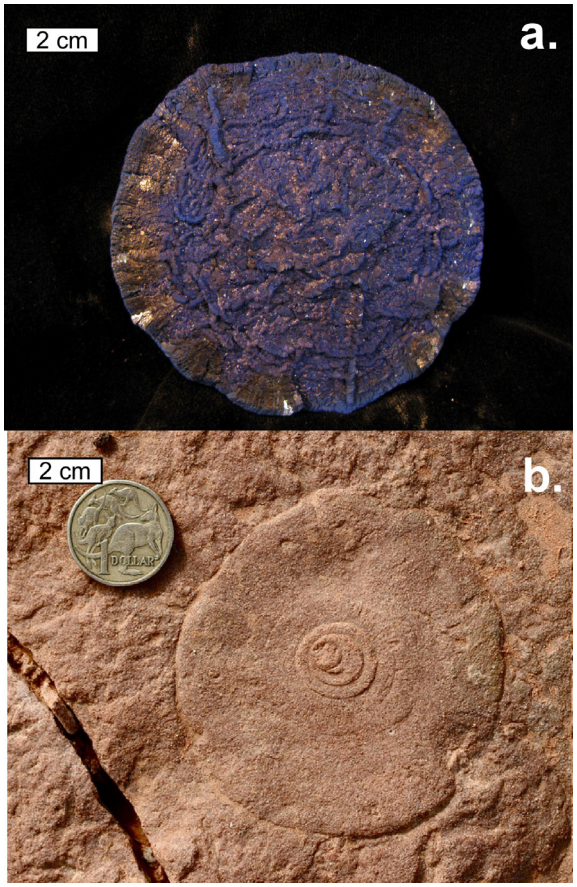

Fig. 7. Morphological comparison of a) typical azurite disk form, and b) *Aspidella terranovica* (photo courtesy ML Droser).

2.3. Isotope analyses and thermometry

Stable isotope analysis for carbon and oxygen was performed on azurite and malachite samples using the standard method of reaction with 100% orthophosphoric acid (H_3PO_4) at 50 °C to release CO_2 gas (e.g., McCrea, 1950; Walters et al., 1972). The resulting CO_2 gas was purified, and then analysed by continuous flow methods on a Finnigan Delta^{plus} isotope ratio mass spectrometer (Spötl and Vennemann, 2003). Detailed descriptions of malachite and azurite sample preparation, analysis techniques, data correction, and data reporting notation are outlined by Melchiorre et al. (1999a) and Melchiorre et al. (2000). Carbon analyses are reported in the usual manner as per mil deviations from the VPDB standard. Results of oxygen analyses are reported as per mil deviation from the VSMOW standard. The precision of the $\delta^{13}C$ value is ±0.09‰, while for $\delta^{18}O$ the precision is ±0.1‰.

Fluid inclusion waters were prepared for oxygen isotope analysis using the standard CO_2 equilibration method (Epstein and Mayeda, 1953). Preparation of water for hydrogen isotope analysis used zinc shavings reacted at 500 °C for 30 min with water to yield hydrogen gas by reduction (Coleman et al., 1982). Precision for $\delta^{18}O$ is ±0.2‰, while the precision for δD is ±1‰.

Previous work by Melchiorre et al. (1999a, 2000) showed that for malachite and azurite, carbon isotope values may be used to determine the source of carbon in the mineral, and oxygen isotope values may be used to establish the temperature of mineral formation. For example, the temperature dependence of malachite is given by the equation:

$$1000\ln\alpha = 2.66 * (10^6/T^2) + 2.66 \quad \text{(Melchiorre etal., 1999a)} \quad (1)$$

While for azurite the relationship is:

$$1000\ \ln\ \alpha = 2.67 * (10^6/T^2) + 4.75 \quad \text{(Melchiorre etal., 2000)} \quad (2)$$

3. Results

XRD analysis of the white clay matrix which hosts the azurite and malachite mineralization determined this is a well-crystallized kaolinite-dominated sandy clay with 2M1 illite (containing less than 3% expandable component). The clay contains a significant quantity of anhedral quartz, presumably inherited from the sedimentary source. Trace tourmaline was also identified in all samples. The red clay was of identical composition, but with the addition of fine grained hematite, an alunite-group mineral, and possible anatase.

The heavy mineral concentrates were found to be rich in fine euhedral, prismatic tourmaline crystals. Chemical analysis of the tourmaline reveals striking chemical zonation (Table 1). Magnesium in the tourmaline ranges from 1.1 to 3.3 wt% in cores, and 4.5–6.5 wt% in rims. Iron in the tourmaline ranges from 6.4 to 10.2 wt% in cores, and 1.9–8.5 wt% in rims. The analyses indicate all cores are schorl and most rim compositions are dravite. Some minor Fe replacement of Al is confirmed for several rim analyses, suggesting higher oxidation in later growth zones. A few analyses have a deficiency in the octahedral cations, indicating a small Li content.

The results of stable isotope analyses are presented in Table 2. Carbon isotope values of azurite range between −9.88 and −7.74‰, while the malachite has a $\delta^{13}C$ value between −12.22 and −11.13‰. The oxygen isotope values of the azurite ranged from 27.66 to 29.54‰, with a value between 27.19 and 27.78‰ for the malachite. The oxygen isotope value of the water of formation, as determined from fluid inclusion extraction, is −5.3‰, and the δD value is −55‰. Using the $\delta^{18}O$ values of the fluid inclusion

Table 1
Probe data for chemistry and formulae of mirco-tourmaline.

	1	2	3	4	5	6	7	8	9	10	11	12	13	14	15	16	17	18	19
(wt%)	Rim	Core	Core	Core	Rim	Rim	Rim	Rim	Rim	Core	Core	Rim	Rim	Rim	Rim	Rim	Rim	Core	Core
SiO_2	37.14	35.66	35.66	35.56	36.88	36.10	36.09	37.59	38.24	34.59	34.33	36.72	38.60	36.19	36.26	35.85	37.92	34.39	34.40
TiO_2	0.07	0.44	0.92	0.59	0.12	0.10	0.09	0.07	0.09	0.81	0.73	0.38	0.03	0.77	0.21	0.49	0.07	0.47	0.84
Al_2O_3	33.00	34.14	33.69	33.96	33.62	31.76	33.78	34.17	31.57	34.18	34.42	31.90	34.86	27.01	32.12	28.94	34.18	34.76	34.42
Cr_2O_3	0.01	0.00	0.02	0.02	0.01	0.02	0.01	0.01	0.01	0.02	0.01	0.00	0.01	0.68	0.01	0.01	0.02	0.00	0.02
FeO	4.06	8.64	8.29	8.55	4.31	6.46	5.45	4.20	5.97	12.38	12.50	5.58	1.68	10.94	7.12	9.81	2.52	12.17	13.06
MgO	9.41	5.44	5.60	5.52	9.07	8.97	8.39	9.01	8.43	2.16	2.19	9.62	10.77	7.39	8.20	7.83	9.58	2.32	1.82
CaO	0.03	0.34	0.45	0.35	0.06	0.05	0.06	0.04	0.05	0.35	0.30	0.38	0.02	0.27	0.07	0.14	0.04	0.25	0.29
MnO	0.00	0.04	0.03	0.01	0.02	0.03	0.00	0.00	0.00	0.06	0.08	0.00	0.02	0.00	0.02	0.00	0.01	0.10	0.10
Na_2O	2.69	1.87	1.84	1.88	2.65	2.94	3.03	2.82	3.12	1.76	1.78	2.62	2.01	3.07	2.47	2.91	1.80	1.75	1.75
K_2O	0.02	0.02	0.02	0.02	0.01	0.01	0.02	0.02	0.02	0.04	0.04	0.02	0.02	0.04	0.02	0.11	0.01	0.04	0.04
B_2O_3	9.76	9.76	9.76	9.76	9.76	9.76	9.76	9.76	9.76	9.76	9.76	9.76	9.76	9.76	9.76	9.76	9.76	9.76	9.76
Total	96.18	96.35	96.28	96.20	96.51	96.22	96.69	97.67	97.26	96.11	96.15	96.98	97.78	96.11	96.26	95.85	95.92	96.02	96.48
Formulae, based on 15 cations excluding Ca, Na, K																			
Si	5.96	5.84	5.85	5.84	5.90	5.86	5.82	5.95	6.00	5.82	5.77	5.89	5.96	6.00	5.88	5.96	6.00	5.77	5.78
Al	6.04	6.16	6.15	6.16	6.10	6.07	6.18	6.05	6.00	6.18	6.23	6.02	6.04	5.35	6.12	5.67	6.00	6.23	6.22
Cr	0.00	0.00	0.00	0.00	0.00	0.00	0.00	0.00	0.00	0.00	0.00	0.00	0.00	0.09	0.00	0.00	0.00	0.00	0.00
Fe^{+3}	0.00	0.00	0.00	0.00	0.00	0.06	0.00	0.00	0.00	0.00	0.00	0.09	0.00	0.56	0.00	0.37	0.00	0.00	0.00
Tet	12.00	12.00	12.00	12.00	12.00	12.00	12.00	12.00	12.00	12.00	12.00	12.00	12.00	12.00	12.00	12.00	12.00	12.00	12.00
Ti	0.01	0.05	0.11	0.07	0.02	0.01	0.01	0.01	0.01	0.10	0.09	0.05	0.00	0.10	0.03	0.06	0.01	0.06	0.11
Al	0.20	0.43	0.37	0.40	0.24	0.00	0.24	0.31	0.00	0.60	0.59	0.00	0.30	0.00	0.02	0.00	0.38	0.64	0.59
Cr	0.00	0.00	0.00	0.00	0.00	0.00	0.00	0.00	0.00	0.00	0.00	0.00	0.00	0.00	0.00	0.00	0.00	0.00	0.00
Fe^{+2}	0.54	1.18	1.14	1.17	0.58	0.81	0.73	0.56	0.80	1.74	1.76	0.66	0.22	0.97	0.97	1.00	0.33	1.71	1.83
Mg	2.25	1.33	1.37	1.35	2.16	2.17	2.02	2.12	2.03	0.54	0.55	2.30	2.48	1.85	1.98	1.94	2.26	0.58	0.45
Mn	0.00	0.01	0.00	0.00	0.00	0.00	0.00	0.00	0.00	0.01	0.01	0.00	0.00	0.00	0.00	0.00	0.00	0.01	0.01
Oct	3.00	3.00	3.00	3.00	3.00	3.00	3.00	3.00	2.84	3.00	3.00	3.00	3.00	2.92	3.00	3.00	2.99	3.00	3.00
Ca	0.00	0.06	0.08	0.06	0.01	0.01	0.01	0.01	0.01	0.06	0.05	0.07	0.00	0.05	0.01	0.02	0.01	0.05	0.05
Na	0.84	0.59	0.59	0.60	0.82	0.93	0.95	0.86	0.98	0.57	0.58	0.81	0.60	1.00	0.78	0.94	0.55	0.57	0.57
K	0.00	0.00	0.00	0.00	0.00	0.00	0.00	0.00	0.01	0.01	0.01	0.00	0.00	0.01	0.00	0.02	0.00	0.01	0.01
Vacancy	0.15	0.34	0.33	0.34	0.16	0.06	0.04	0.13	0.01	0.35	0.36	0.12	0.39	-0.06	0.20	0.01	0.44	0.38	0.37
A	0.85	0.66	0.67	0.66	0.84	0.94	0.96	0.87	0.99	0.65	0.64	0.88	0.61	1.06	0.80	0.99	0.56	0.62	0.63
Total	15.85	15.66	15.67	15.66	15.84	15.94	15.96	15.87	15.83	15.65	15.64	15.88	15.61	15.98	15.80	15.99	15.56	15.62	15.63
Mg/Mg + Fe	0.805	0.529	0.546	0.535	0.790	0.727	0.733	0.793	0.716	0.237	0.238	0.778	0.920	0.655	0.672	0.661	0.871	0.254	0.199
Li	0.000	0.000	0.000	0.000	0.000	0.000	0.000	0.000	0.162	0.000	0.000	0.000	0.000	0.079	0.000	0.000	0.008	0.000	0.000

Table 2
Stable isotope data for malachite and azurite samples used in this study.

Sample Number	Mineral	$d^{13}C$ (VPDB) (‰)	$d^{18}O$ (VSMOW) (‰)	Oxygen isotope thermometry temperature of formation estimate (°C)
A3	Azurite Disk	−8.28	28.13	34.0
A4	Azurite Disk	−8.58	28.13	34.0
A7	Azurite Disk	−8.90	28.27	33.2
A8	Azurite Disk	−8.58	27.85	35.5
A9	Azurite Disk	−8.91	28.32	33.0
A10	Azurite Disk	−7.74	28.12	34.0
A11	Azurite Disk	−9.28	27.66	36.5
A12	Azurite Disk	−7.94	28.21	33.5
A13	Azurite Disk	−8.74	28.13	34.0
A15	Azurite Disk	−7.96	28.46	32.2
A14	Azurite Disk	−9.23	27.84	35.5
EM4	Azurite Disk	−10.06	27.40	37.9
EM1	Malachite Nodule	−12.22	27.78	24.3
EM2	Malachite Nodule	−11.59	27.55	25.5
M5	Malachite Nodule	−11.13	27.19	28.6
EM3	Azurite Crystals	−9.25	29.08	29.1
EM4	Azurite Crystals	−9.49	28.89	30.0
A6	Azurite Crystals	−9.88	29.54	26.8

Table 3
Chemical and isotopic composition of azurite-hosted fluid inclusions from the Malbunka deposit, with comparison to average seawater values from Chester and Jickells (2012).

	Ca (ppm)	Mg (ppm)	Na (ppm)	K (ppm)	Cl (ppm)	SO_4 (ppm)	Ba (ppm)	B (ppm)	Sr (ppm)	TDS (ppm)
Azurite Inclusion Water	45	20	1100	17	1000	18	0.19	42	6.4	2700
[1]Seawater	411	1250	10,800	392	19,400	940	0.021	4.45	8.1	35,000
	$d^{18}O$ ‰ (VSMOW)		dD ‰ (VSMOW)		Na/Cl	SO_4/Mg		B/Ba		Na/Ca
Azurite Inclusion Water	−5.3		−55.0		1.1	0.9		221		24
Seawater	[2] 0.0		[2] 0.0		0.6	0.8		212		26

[1] Chester and Jickells (2012).
[2] Assumed by definition, VSMOW.

water and the copper carbonate minerals, it is possible to calculate temperatures of formation using the corresponding fractionation factors (α). These fractionation factors can then be used with the azurite and malachite thermometry equations (Eqs. (1) and (2)) to determine a temperature of formation. The oxygen isotope thermometry results suggest that the azurite disks formed between temperatures of 32.2–37.9 °C, azurite crystals formed between 26.8 and 30.0 °C, while malachite formed at 24.3–28.6 °C.

Results of chemical analysis of azurite-hosted fluid inclusions are presented in Table 3. The fluid inclusion waters are rich in boron, chlorine, and other elements suggestive of dilute oil basin formation fluids.

4. Discussion

4.1. Geology and mineralogy

Copper carbonate minerals at Malbunka have been divided into three groupings for the purpose of this study. The most common occurrence of azurite is a discoidal form, comprised of numerous small flat crystals of azurite arranged in radial and concentric forms. These disks occupy bedding planes, relic thrust fault planes, and joints in the white and less commonly in the red kaolinite-dominated clay host rock. These disks occasionally display interbedding relicts of the original clay host. Dark blue azurite disks are relatively free of solid-phase mineral inclusions, but do contain fluid inclusions. The colour of the light blue azurite disks is caused by incorporation of fine white clay interstitial to micro-azurite crystals during crystallisation.

Azurite is also noted in lesser abundance as more equant or spheroidal crystal clusters. These clusters form from the radial growth of terminated azurite crystals from a central nucleation point. These clusters of azurite crystals are quite similar to the azurite disks, with the exception being coarser crystal size and more 3-dimensional form. Malachite is much less common, and is found as either finely-crystalline masses often with a lobate spheroidal to discoidal form, or rarely as pseudomorphous replacements of azurite. The observed paragenetic sequence is microcrystalline azurite disks, followed by azurite crystal cluster nodules, followed by malachite.

The clay-rich sandstone which forms both the upper and lower boundary of the azurite-bearing clay, and even the clay bed itself, contain abundant sediment deformation features such as recumbent folds, slumping, micro-faulting, and flow structures (Fig. 8) that may be injectites or seismites caused by earthquake shock during sedimentation (e.g., Shi et al., 2007). Many of these soft sediment injection structures are difficult to see in the field, due to a lack of contrast between the shades of off-white clay involved.

There is ample evidence that copper bearing fluids penetrated into the upper and lower layers of the kaolinite lens next to the sandstone, and to a lesser extent into the central thickest part of the kaolinite (Fig. 8c). Azurite disks and other forms of copper carbonate are observed forming directly adjacent to fluid flow structures. Thrust planes are common in the hanging wall area of the kaolinite lens where imbrication structures are evident over distances of several meters. Thrusting preceded copper mineralisation and continued after the mineralising event, which along with the injectite events, demonstrates the dynamic environment under which most of the mineralisation took place.

4.1.1. Injectites

Three distinct over-pressure events, characterized by injectite structures, have been identified within the kaolinite lens (Fig. 8). These events followed shock induced sediment slumping of sandstone and kaolinite (Fig. 8a). The first event was characterised by eruption of streamers of white clay into higher levels of the kaolinite lens. Injectites from this event are difficult to see, due to the lack of contrast in the off-white layers (Fig. 8b).

The second event is characterised by hydraulic fracturing of the kaolinite close to the hanging wall and the opening of vertical fractures in the clay followed closely by crystallisation of azurite (Fig. 8c). Azurite cementation of hydraulically-fractured kaolinite is also noted (Fig. 8d).

The third event consists of sandstone injectites penetrating into the kaolinite from the hanging wall (Fig. 8e). Injectites associated with this event deform pre-existing azurite which has crystallised in the plane of relic thrust faults (Fig. 8e, note azurite layer offset by the injectite near the tip of the pick). Late-stage micro faulting occurs during this phase (Fig. 8f). Malachite is present along the edge of the sandstone injectite, suggesting formation late in the paragenetic sequence.

Structures associated with these events indicate that fluid pressures built up and were released explosively at least three times within the deposit. If the structures were purely a response to shearing or compressional forces, the kaolinite would have flowed and smeared like plasticine and not formed sharp vertical contacts with randomly-oriented clay and sandstone fragment inclusions. The hydraulic overpressure events required to produce these structures within a sedimentary sequence are not near surface phenomena suggesting azurite formation is not related to passive near surface copper sulfide oxidation events that normally precede azurite crystallisation.

These types of injection structures may be seismites, which record seismic activity associated with basin dewatering and compaction (e.g., Seilacher, 1969). These same structures are noted for deep sediments within petroleum basins around the world (e.g., Thompson et al., 2007; Kane, 2010).

4.1.2. Resemblance to fossils

The possibility of the azurite disks representing Ediacaran fauna (Fig. 7) has been discounted by field evidence. While the rocks at the Malbunka deposit are of appropriate age (Lindsay, 1987; Mapstone and McIlroy, 2006), the form of the proposed fauna represented (*Dickinsonia costata* and *Aspidella terranovica*) is inconsistent with the azurite disks. For example, while *D. costata* is often of appropriate size, it commonly displays an elongate form with bilateral symmetry unlike the uniformly round azurite disks. Similarly, *A. terranovica* has superficial features that are similar to the azurite disks, such as concentric rings and centripetal rays. The inferred remnant of a holdfast stalk (e.g., MacGabhann, 2007) on *A. terranovica*, evident as a raised central pimple, is also present on some azurite disks. However, the size of most *A. terranovica* specimens is much smaller than the azurite disks, at only 0.4–1 cm (e.g., Narbonne, 2005). Population densities for these fauna are also inconsistent with observed densities of azurite disks (Fig. 3d). These is also structural evidence that the azurite disks are not fossils, namely that they are occasionally observed to incorporate relict bedding structures, and cross-cut bedding along joints. And while an Ediacaran organism, *Arumberia banksi*, has been reported for local rocks interpreted to be the lateral equivalents of the Namatjira Formation (Glaessner and Walter, 1975), it was later re-interpreted as having formed from the action of currents on a cohesive muddy substrate (McIlroy and Walter, 1997).

4.2. Carbon sourcing

Carbon isotope values of the azurite and malachite from the Malbunka deposit are low, and inconsistent with carbon from the local marine carbonate units or the atmosphere (Fig. 9). Volcanic CO_2 carbon isotope values are also insufficient to explain the whole range of observed values in these copper carbonate minerals. The

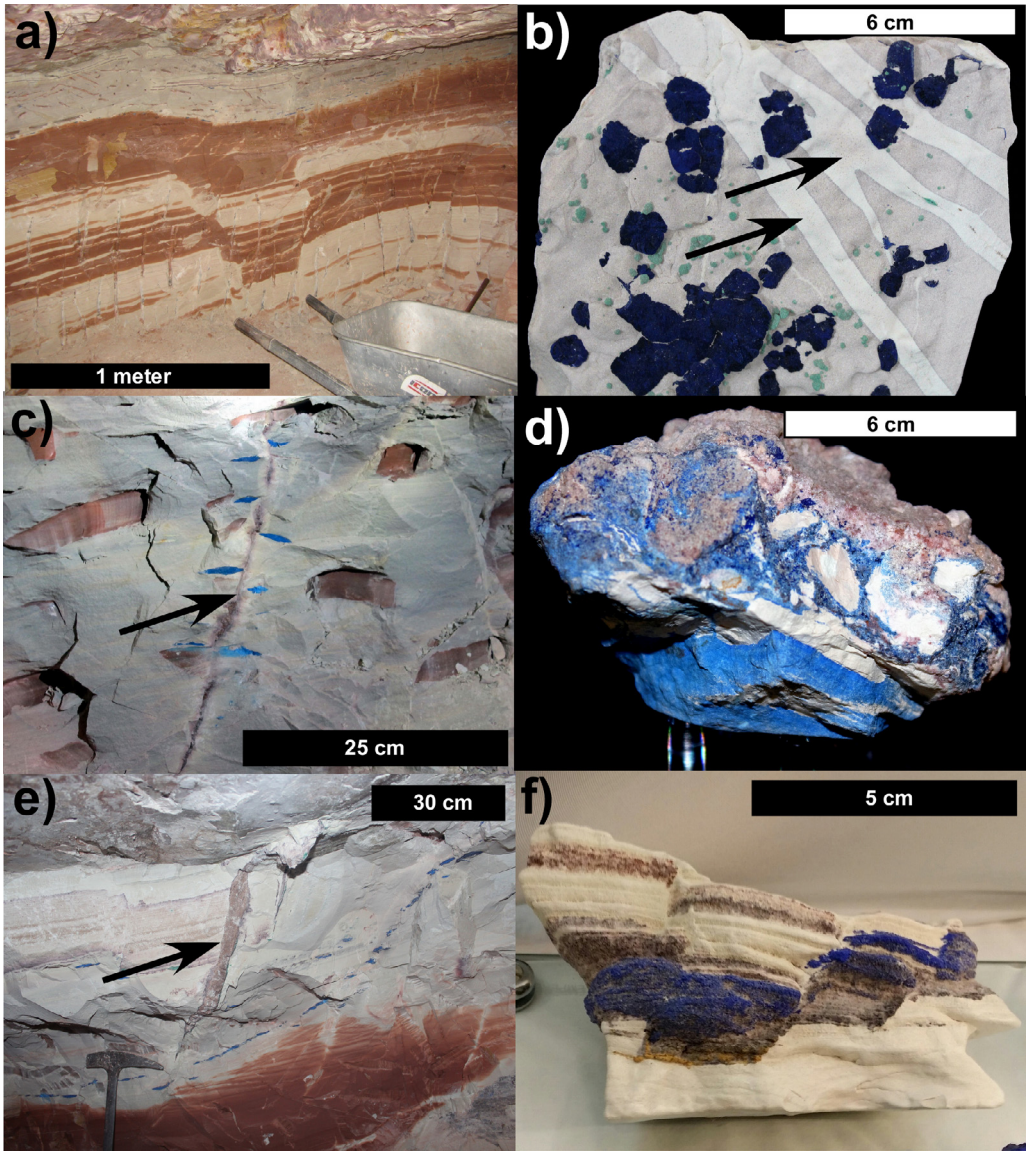

Fig. 8. Sediment deformation structures a) Sediment bed slumping (approximately 2 m field of view, wheelbarrow for scale). b) Light white injectites (black arrows) cut off-grey-white clay matrix. Specimen is 12 cm long. c) Cross-sectional view of azurite disks forming directly adjacent to a fluid pathway joint (black arrow). Photo is 50 cm across. d) Azurite-cemented breccia specimen (9 cm long) from fluid conduit zone beneath clay unit. e) Sediment injection structure, cross-cutting bedding (black arrow above rock hammer). f) Late stage injectites and associated faulting cut azurite mineralization (specimen is 10 cm).

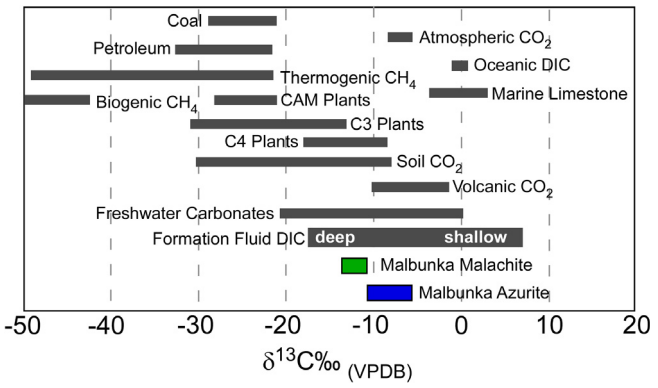

Fig. 9. Carbon isotope values of Malbunka deposit azurite and malachite, relative to potential carbon sources. Data fields other than azurite and malachite are from Sharp (2007) and references therein. Formation fluid distinctions between shallow and deep are based upon Bailey et al. (1973) and Carothers and Kharaka (1980).

best fit for these values is carbon from deep groundwater basins, including formation brines associated with petroleum. However, there are many potential origins for carbon within these deep basins (e.g., Fontes, 1985). The closest match for the observed $\delta^{13}C$ values is for a source dominated by organic carbon (e.g., Jiráková et al., 2010), or soil CO_2 (e.g., Rose et al., 1996). Respectively, these potential carbon sources would be consistent with a deep or very shallow sedimentary basin setting. However, in oil field brines the $\delta^{13}C$ values are observed to be lighter in the deeper portions of the basin, which is attributed to oxidative microbial degradation of petroleum (e.g., Bailey et al., 1973; Carothers and Kharaka, 1980). If true, this would suggest that Malbunka azurite and malachite formed after the period of petroleum maturation, from a deep biological carbon source.

In addition, there is a positive correlation between $\delta^{13}C$ and $\delta^{18}O$ values for Malbunka copper carbonates (Fig. 10, Table 2). Such positive correlations in carbonates have been interpreted by many as a record of diagenesis deep within a sedimentary sequence (e.g.,

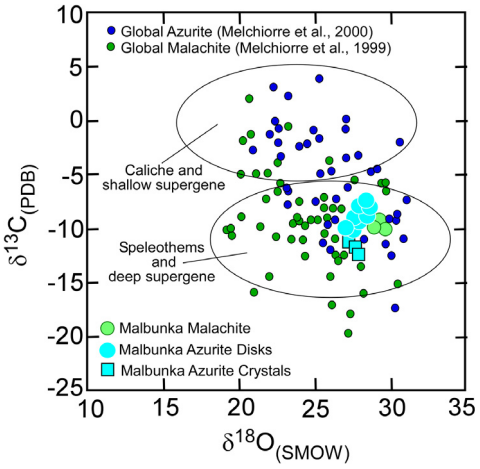

Fig. 10. Carbon vs oxygen isotope plot, showing relationships between Malbunka copper carbonates, global azurite and malachite, and inferred sources from Melchiorre et al., 2000.

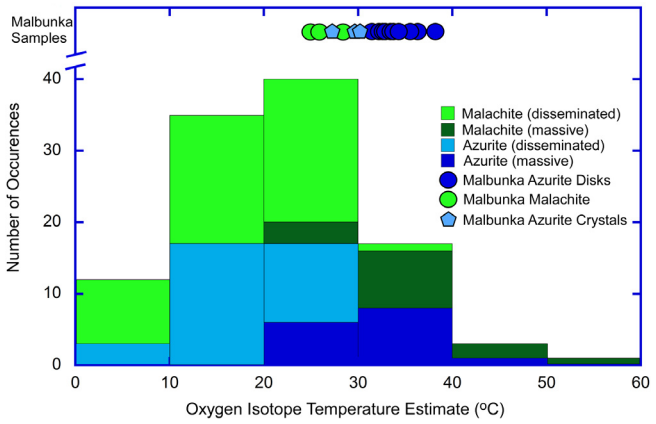

Fig. 11. Distribution of oxygen isotope thermometry estimates for malachite (Melchiorre et al., 1999a) and azurite (Melchiorre et al., 2000) samples from around the world, showing relative temperatures for samples from the Malbunka deposit.

Allan and Matthews, 1982). The Malbunka copper carbonates plot within the field of deep supergene copper carbonate samples, and speleothem carbonates.

4.3. Isotope thermometry

The geothermometers in Eqs. (1) and (2) were used in conjunction with the results of oxygen isotope analyses for copper carbonate minerals to produce estimates of the temperatures at which the azurite and malachite formed (Table 2). A $\delta^{18}O$ value of −5.3‰, derived from fluid inclusion work, was used as the water of equilibration. It is acknowledged that this $\delta^{18}O$ value would be more robust if additional measurements had been made, as it is possible that oxygen isotope exchange histories and different inclusion types may produce a range of values. However, the large volume of pure azurite which was required for crushing stage isotope measurements limited our ability to do so. Nevertheless, we believe that the large volume of azurite which was used for the measurement works to advantage, as it represents an averaging of many inclusion types and histories, and is likely to be representative of a true bulk inclusion water $\delta^{18}O$ value.

These isotope geothermometry temperatures are all well above the recorded ambient air temperatures, and often above even the seasonal extreme records (Australian Bureau of Meterology, 2016). This suggests that the copper carbonate minerals formed in an environment with additional heat beyond the influence of the atmosphere. A volcanic source of heat is not likely, based upon local geology and carbon isotope evidence. Heat from exothermic geochemical or biological decomposition of sulfides is a possible source (e.g., Melchiorre and Williams, 2001), but would require a much larger body of massive sulfide proto-ore than would have been geologically possible for the deposit. A plot of malachite and azurite oxygen isotope temperature estimates from around the world (Fig. 11) shows that samples from disseminated deposits have lower temperatures than samples from deposits where very large masses of sulfide minerals have been replaced by copper carbonate masses. It is presumed that heat from oxidation of concentrated sulfides produces this distribution. The range of temperature estimates for the copper carbonate minerals of the Malbunka deposit are consistent with azurite formation from a massive sulfide-type ore body, while malachite is consistent with a disseminated host. However, there is no geological evidence for a concentrated mass of sulfides at the Malbunka deposit. Quite the contrary, the copper carbonates show ample evidence of a disseminated distribution from a highly remobilized source (e.g., Figs. 2d and 7c).

The most reasonable source of heat within the rocks of the Amadeus Basin is the geothermal heat related to the local ambient gradient. Cull and Conley (1983) state that major sedimentary basins in Australia have between 10 and 40 °C of temperature increase per kilometer of depth in the basin. However, detailed study of the Amadeus Basin indicates this basin actually has a lower value of 10–25 °C due to the thermal conductivity properties of the rocks (Beardsmore, 2007). Given this geothermal gradient, the isotope thermometry estimates which are 5–16 °C above ambient temperatures would suggest the copper carbonates formed at a depth in this basin between 0.3 and 1.6 km. These estimates are based on the assumption that the modern geothermal gradient is broadly similar to the gradient in the past, as the thermal properties of the rock have not changed significantly. These temperature estimates are also supported by fluid inclusion studies of halite from other units of the Amadeus Basin, which suggest early diagenesis occurred at temperatures of 60–100 °C (Kovalevych et al., 2006). The possibility does exist that the Malbunka azurite formed slightly closer to the surface at a time in the past when global atmospheric temperatures were higher. However, given that the azurite formed in a diagenetic context, and the relatively minimal depth to which atmospheric temperature would have an impact (e.g., Domínguez-Villar et al., 2015), we consider this effect to be negligible.

4.4. Tourmaline qualitative thermometry

The kaolinite-dominated white and red clay associated with the Malbunka azurite deposit contains abundant, fine-grained tourmaline crystals (Fig. 12). These euhedral to subhedral crystals range from 10 to 75 μm in length and have compositional, textural, and contextual geological data consistent with authigenic formation under oxidizing conditions at low temperature, similar to tourmaline reported from the cap rock of salt domes (Henry et al., 1999). Authigenic tourmaline has been widely reported to occur within clay, potash, halite, and anhydrite associated with evaporite deposits (e.g., Mügge, 1913; Popov and Sadykov, 1962; Hiller and Keller, 1965). There is no evidence of fracturing or weathering of the tourmaline crystals from Malbunka that would suggest a detrital or volcanic origin. Significant intracrystalline geochemical variation was noted for Malbunka micro-tourmaline (Figs. 12 and 13; Table 1). The Malbunka crystals are alkali-group tourmaline similar to tourmaline from Challenger Knoll caprock, and evaporate and *meta*-evaporite deposits elsewhere in the world (e.g., Hawthorne and Henry, 1999). Formula calculations indicate the tourmaline is

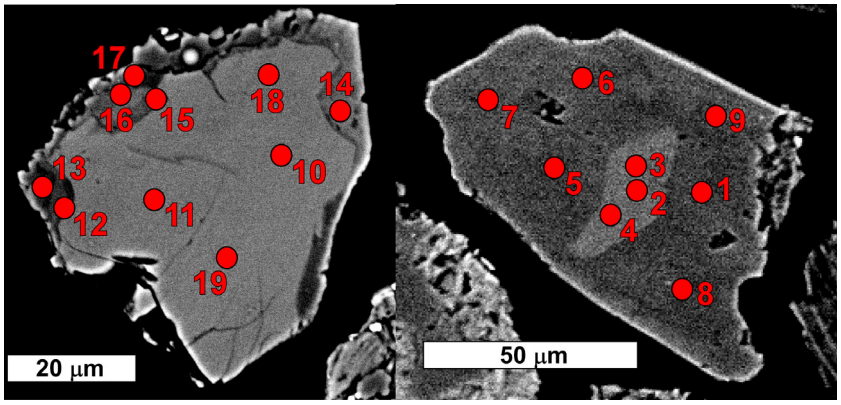

Fig. 12. Scanning Electron backscatter images of micro-tourmaline crystals, showing locations of probe analyses in Table 1.

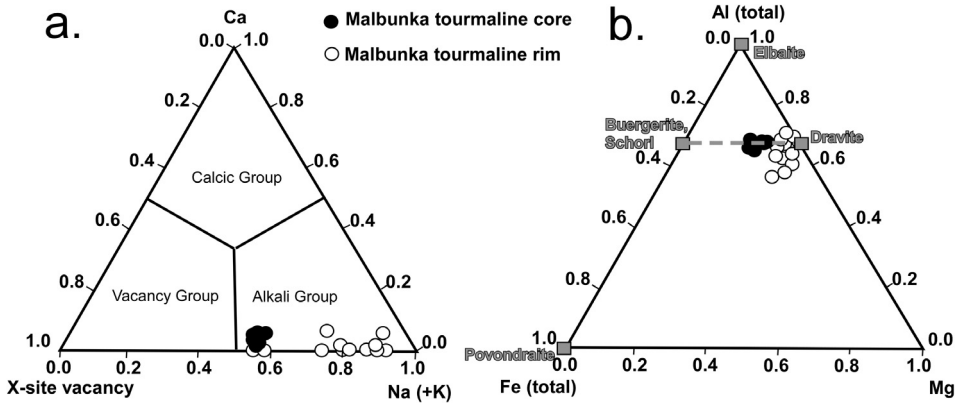

Fig. 13. Chemical classification of micro-tourmaline from the Malbunka deposit.

largely Al-deficient, suggesting replacement of Al by Fe^{3+} in tetrahedral sites. The cores and many rims of Malbunka tourmaline plot along the schorl-dravite join, while some rims blot below it (Fig. 13). These tourmalines have compositional trends similar to a solid solution between ferrian "oxy-dravite" and povondraite reported for salt dome cap rock (Hawthorne and Henry, 1999). Substantial element zonation is noted in different sectors of the tourmaline, but the most significant is high Fe with strong internal variation. Elevated Fe content in tourmaline has been noted for oxidized evaporate rocks (Walenta and Dunn, 1979; Mattson and Rossman, 1984; Grice et al., 1993; Jiang et al., 1997). Significant compositional variation between tourmaline crystals has been noted for some localities (e.g., Cavarretta and Puxeddu, 1990), but only salt dome cap rock tourmalines exhibit this same range of variation within single grains (Henry et al., 1999).

It is suggested by many that surface energies play a key role in chemical zonation within tourmaline and other minerals in the low temperature environment (e.g., Reeder and Prosky, 1986; Fouke and Reeder, 1992; Rakovan and Waychunas, 1996). However, the surface effects upon sector zoning decrease significantly with increasing temperature (Henry and Dutrow, 1992). Geochemical analysis of the micro-tourmaline from Malbunka reveal elemental abundances and chemical zonation consistent with low temperature authigenic formation from evaporite sources, consistent with formation ~1 km deep within the Amadeus Basin.

4.5. Fluid inclusion chemistry

Fluid inclusion waters from Malbunka azurite have elevated element concentrations and light stable isotope values consistent with fluids from petroleum basins (Table 3). Azurite is nearly opaque, however we presume that the majority of inclusions are primary given thermal and textural relations. The inclusion fluid is enriched in boron, and has key element ratios consistent with a seawater origin, similar to values reported for evolved formation fluids that have experienced meteoric dilution through seismic pumping (e.g., Melchiorre et al., 1999b). Ca excess/Na deficit in these fluids do not suggest albitization reactions within the basin (Davisson and Criss, 1996). Ratios of key elements in the inclusion waters are similar to seawater, with the exception of Na/Cl. Chlorine deficit may result from precipitation of the copper chloride mineral atacamite, which is known to have occured within the distal portions of the deposit. The chemical differences between the azurite inclusion water and halite inclusion water (Kovalevych et al., 2006) most likely results from the different host lithologies, and timing of mineralization. The oxygen and hydrogen stable isotope values of the Malbunka azurite inclusion fluid are consistent with local meteoric dilution of formation fluid with a seawater origin, and subsequent water-rock interaction, similar to formation fluids from sedimentary basins around the world (e.g., Clayton et al., 1966; Wilson and Long, 1993; Moldovanyi et al., 1993).

4.6. Environment of deposit formation

Following their deposition within the Amadeus Basin, these sediments were subjected to diagenetic processes that produced dewatering, lithification, and mineralization. It is not known what role, if any, the formation of the Amadeus aulacogen (Rutland, 1973) may have had on copper mineralization (Sawkins, 1976). During early diagenesis, halite was mobilized and recrystallized

at temperatures of 60–100 °C (Kovalevych et al., 2006). Water-rock interaction modified pore fluid composition and altered host lithology through kaolinization with associated micro-tourmaline formation. During this time, compaction and associated dewatering elevated pore pressures to between hydrostatic and lithostatic. The highly-contrasting lithologies of the Amadeus Basin, and the discrete nature of their structures suggest that initial compaction produced compartmentalization and significant localized overpressure environments. Fluid flow through this type of poorly-connected system, with limited fluid mixing, is known to juxtapose fluids with significantly different chemistries (e.g., Rowland et al., 2008). When fluid pressures exceeded the failure envelope of the confining lithology, the result was very rapid fluid migration, recorded by a variety of dewatering structures such as injectites (Fig. 8). These events permitted mixing of fluids with vastly different chemistries, and significantly altered local pressure. We propose that a copper-rich formation fluid from a deep source was released by these events to move upward and be trapped by the kaolinite-rich formation, where it mixed with a more dilute and CO_2-rich meteoric fluid. This mixing produced T-pH-p[CO_2] conditions which permitted azurite mineralization directly adjoining the fluid flow structures (Fig. 14). However, at this time early in dewatering and depressurization, the compaction and fluid pressure dictated mostly 2-dimensional growth, similar to "pyrite dollars" which form as concretions during diagenetic conditions in some black shales elsewhere in the world. This population of azurite mineralization records isotopic equilibration temperatures 5–16° C above ambient temperatures which corresponds to a basin depth of 0.3–1.6 km. As dewatering and depressurization progressed, azurite was able to crystalize under more equalized pressure as spheroidal crystal clusters with attendant lower isotope thermometry estimates. At some point, the depressurization and depletion of the CO_2 source produced lower p[CO_2] conditions which shifted into the malachite stability field (Fig. 14). This last phase of mineralization is recorded by discoidal malachite masses, some pseudomorphously replacing pre-existing azurite at near ambient surface temperatures.

A significant factor in the creation of this deposit is the occurrence of an impermeable clay unit. The association of kaolinite-dominated white and red clays with azurite formation has been noted in many other deposits (e.g., Grant, 1989; Melchiorre and Enders, 2003). It is suggested that the relatively impermeable clay enhances p[CO_2] levels by creating a comparatively closed system that can reach the high levels above atmospheric required for azurite formation. The occurrence of impermeable clay units could provide a useful exploration tool in identification of economic copper targets. These clay-associated azurite deposits, such as the Northwest Extension at Morenci, Arizona, USA, can contain globally significant quantities of copper. The model in the Malbunka case has clay traps above fracture zones associated with halite-rich diapirs.

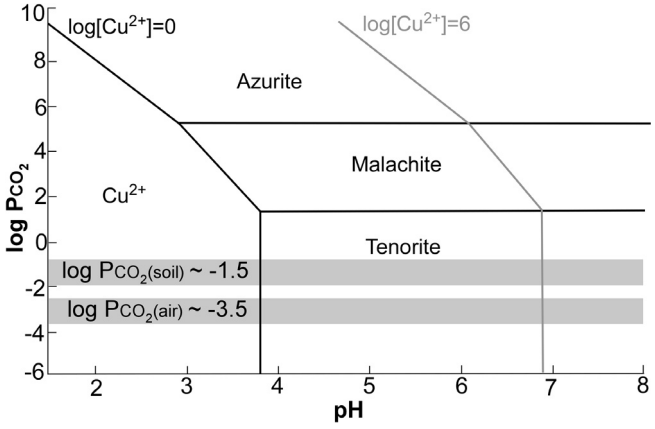

Fig. 14. Stability relations of malachite and azurite in logPCO_2 – pH space, after Kiseleva et al. (1992).

5. Conclusions

Azurite and malachite from the Malbunka deposit appear to form as primary ore minerals, rather than as secondary replacement of sulfides as is typical of other copper carbonate deposits around the world. Fluid flow structures and fluid inclusion data indicate formation of azurite and malachite occurred due to mixing between a deep basin formation fluid rich in copper, and more shallow meteoric-diluted fluids rich in carbonate. Stable isotope values of these minerals and micro-tourmaline chemistry suggest formation of copper carbonates occurred 0.3–1.6 km deep with a sedimentary basin under conditions similar to diagenetic carbonates. The unusual growth habit of the azurite disks is not due to fossil replacement, but rather an artefact of hydrostatic to lithostatic fluid pressure related to diagenesis. The paragenetic sequence of mineralization is azurite disks at higher P and T than later 3-dimensional azurite crystal clusters, followed by malachite formation at near ambient temperatures and near surface conditions. The role of clay in creating overpressured conditions, and retaining the high pCO_2 values required for azurite formation require additional investigation due to the potential importance in understanding the genesis of primary copper carbonate ore bodies.

Acknowledgements

Instrumentation was provided and supported by the National Science Foundation, EAR-0115884 and EAR-0941106. XRF instrumentation was provided by a grant from the W.M. Keck Foundation. Support was also provided by a NASA Astrobiology Institute Minority Institution Research Sabbatical (NAI-MIRS) program award to the lead author, and an institutional grant by CSUSB. The lead author thanks his colleagues in the Minority Institution Astrobiology Collaborative (MiAC) for creating the positive and supportive environment in which this research was possible. We thank Ray Grant for valuable discussions of geology, and H. Albert Gilg for assistance with clay mineralogy. R. Bottrill publishes with the permission of the Tasmanian Director of Mines.

References

Allan, J.R., Matthews, R.K., 1982. Isotope signatures associated with early meteoric diagenesis. Sedimentology 29, 797–817.
Ambrose, G., 2006. Northern Territory of Australia, onshore hydrocarbon potential, 2006. Northern Territory Geological Survey Record 2006-003.
Armstrong, J.T., 1988. Quantitative analysis of silicates and oxide minerals: comparison of Monte-Carlo, ZAF and Phi–Rho–Z procedures. In: Newbury, D. E. (Ed.), Proceedings of the Microbeam Analysis Society. Microbeam Analysis Society, San Francisco, pp. 239–246.
Australian Bureau of Meterology, 2016. <http://www.bom.gov.au> (accessed 20 February 2016).
Bailey, N.J.L., Krouse, H.R., Evans, C.R., Rogers, M.A., 1973. Alteration of crude oil by waters and bacteria–evidence from geochemical and isotope studies. AAPG Bull. 57, 1276–1290.
Beardsmore, G., 2007. Geothermal energy potential of the Northern Territory. Northern Territory Geological Survey Record 2007-004.
Carothers, W.W., Kharaka, Y.K., 1980. Stable carbon isotopes of HCO_3 – in oil-field waters—implications for the origin of CO_2. Geochim. Cosmochim. Acta 44, 323–332.
Cavarretta, G., Puxeddu, M., 1990. Schorl-dravite-ferridravite tourmalines deposited by hydrothermal magmatic fluids during early evolution of the Larderello geothermal field, Italy. Econ. Geol. 85, 1236–1251.
Chester, R., Jickells, T., 2012. Marine Geochemistry. Wiley-Blackwell Publishing, Hoboken, NJ.

Clayton, R.N., Friedman, I., Graf, D.L., Mayeda, T.K., Meents, W.F., Shimp, N.F., 1966. The origin of saline formation waters: isotopic composition. J. Geophys. Res. 71, 3869–3882.
Coleman, M.L., Shepard, T.J., Rouse, J.E., Moore, G.R., 1982. Reduction of water with zinc for hydrogen isotope analysis. Anal. Chem. 54, 993–995.
Cook, P.J., 1968. Henbury, Northern Territory 1:250,000 geological map series, explanatory notes. Northern Territory Geological Survey SG53-01.
Cull, J.P., Conley, D., 1983. Geothermal gradients and heat flow in Australian sedimentary basins. J. Aust. Geol. Geophys. 8, 329–337.
Davisson, M.L., Criss, R.E., 1996. Na-Ca-Cl relations in basinal fluids. Geochim. Cosmochim. Acta 60, 2743–2752.
Domínguez-Villar, D., Lojen, S., Krklec, K., Baker, A., Fairchild, I.J., 2015. Is global warming affecting cave temperatures? Experimental and model data from a paradigmatic case study. Clim. Dyn. 45 (3–4), 569–581.
Dyson, I.A., Marshall, T.R., 2005. Neoproterozoic salt nappe complexes and salt-withdrawal minibasin in the Amadeus Basin. In: Proceedings of the Central Australian Basins Symposium (CABS). Alice Springs, Northern Territory, pp. 16–18.
Edgoose, C.J., 2013. Geology and Mineral Resources of the Northern Territory. In: Ahmad, M., Munson, T.J. (Eds.), Amadeus Basin. Northern Territory Geological Survey Special Publication 5.
Epstein, S., Mayeda, T., 1953. Variation of ^{18}O content of waters from natural sources. Geochim. Cosmochim. Acta 4, 213–224.
Fontes, J.C., 1985. Some considerations on ground water dating using environmental isotopes. In: Hydrogeology in the Service of Man. Memoires of the 18th Congress of the International Association of Hydrogeologists, pp. 118–151. Cambridge.
Fouke, B.W., Reeder, R.J., 1992. Surface structural controls on dolomite composition: evidence from sectoral zoning. Geochim. Cosmochim. Acta 56, 4015–4024.
Freeman, M.J., Shaw, R.D., Offe, L.A., 1987. A field guide to geological localities in the Alice Springs region. Northern Territory Geological Survey Technical Report GS 87/9.
Girardi, O., 2012. In-Situ Stresses and Palaeostresses around Salt Diapirs: a Structural Analysis from the Gulf of Mexico and Amadeus Basin, Central Australia (Honours thesis). University of Adelaide.
Glaessner, M.F., Walter, M.R., 1975. New Precambrian fossils from the Arumbera Sandstone, Northern Territory, Australia. Alcheringa 1, 59–69.
Goldstein, J.I., Newbury, D.E., Echlin, P., Joy, D.C., Lyman, C.E., Lifshin, E., Sawyer, L.C., Michael, J.R., 2003. Scanning Electron Microscopy and X-ray Microanalysis: A Text for Biologists, Materials Scientists, and Geologists. Plenum Press, New York.
Grant, R., 1989. The Blue Ball mine, Gila County, Arizona. Mineral. Rec. 20, 447–450.
Grice, J.D., Ercit, T.S., Hawthorne, F.C., 1993. Povondraite: a redefinition of the tourmaline ferridravite. Am. Mineral. 78, 433–436.
Haines, P.W., Hand, M., Sandiford, M., 2001. Palaeozoic synorogenic sedimentation in central and northern Australia: a review of distribution and timing with implications for the evolution of intracontinental orogens. Aust. J. Earth Sci. 48, 911–928.
Hawthorne, F.C., Henry, D.J., 1999. Classification of the minerals of the tourmaline group. Eur. J. Mineral. 11, 201–215.
Henry, D.J., Dutrow, B.L., 1992. Tourmaline in a low grade clastic metasedimentary rocks: an example of the petrogenetic potential of tourmaline. Contrib. Mineral. Petrol. 112, 203–218.
Henry, D.J., Kirkland, B.L., Kirkland, D.W., 1999. Sector-zoned tourmaline from the cap rock of a salt dome. Eur. J. Mineral. 11, 263–280.
Hiller, J.E., Keller, P., 1965. Untersuchungen an den Losern der Kalisalzlagerstatte Buggingen. Kali Steinsalz 4, 190–203.
Jiang, S.Y., Palmer, M.R., Peng, Q.M., Yang, J.H., 1997. Chemical and stable isotopic compositions of Proterozoic metamorphosed evaporites and associated tourmalines from the Houxianyu borate deposit, eastern Liaoning, China. Chem. Geol. 135, 189–211.
Jiráková, H., Huneau, F., Hrkal, Z., Celle-Jeanton, H., LeCoustumer, P., 2010. Carbon isotopes to constrain the origin and circulation pattern of groundwater in the north-western part of the Bohemian Cretaceous Basin (Czech Republic). Appl. Geochem. 25, 1265–1279.
Kane, I.A., 2010. Development and flow structures of sand injectites: the Hind Sandstone Member injectite complex, Carboniferous, UK. Marine Petrol. Geol. 27, 1200–1215.
Kiseleva, I.A., Ogorodova, L.P., Melchakova, L.V., Bisengalieva, M.R., Becturganov, N. S., 1992. Thermodynamic properties of copper carbonates—malachite $Cu_2(OH)_2CO_3$ and azurite $Cu_3(OH)_2(CO_3)_2$. Phys. Chem. Miner. 19, 322–333.
Kovalevych, V.M., Marshall, T., Peryt, T.M., Petrychenko, Y., Zhukova, S.A., 2006. Chemical composition of seawater in Neoproterozoic: results of fluid inclusion study of halite from Salt Range (Pakistan) and Amadeus Basin (Australia). Precambr. Res. 144, 39–51.
Laurie, J.R., Nicoll, R.S., Shergold, J.H., 1991. Ordovician siliciclastics and carbonates of the Amadeus Basin, Northern Territory. Bureau of Mineral Resources, Australia Record 1991/049.
Lindsay, J.F., 1987. Sequence stratigraphy and depositional controls in late Proterozoic-Early Cambrian sediments of Amadeus Basin, central Australia. AAPG Bull. 71, 1387–1403.
MacGabhann, B.A., 2007. Discoidal fossils of the Ediacaran biota: a review of current understanding. Geol. Soc., London 286, 297–313. Special Publication.
Mapstone, N.B., McIlroy, D., 2006. Ediacaran fossil preservation: taphonomy and diagenesis of a discoid biota from the Amadeus Basin, central Australia. Precambr. Res. 149, 126–148.
Mattson, S.M., Rossman, G.R., 1984. Ferric iron in tourmaline. Phys. Chem. Miner. 11, 225–234.
McIlroy, D., Walter, M.R., 1997. A reconsideration of the biogenicity of Arumberia banksi of Glaessner & Walter. Alcheringa 21, 79–80.
McCrea, J.M., 1950. On the isotopic chemistry of carbonates and a paleotemperature scale. J. Chem. Phys. 18, 849–858.
McLaughlin, D., Grant, R., 2012. Azurite suns from the Malbunka Copper Mine Northern Territory Australia. Rock Miner. 87, 490–501.
Melchiorre, E.B., Criss, R.E., Rose, T.P., 1999a. Oxygen and carbon isotope study of natural and synthetic malachite. Econ. Geol. 94, 245–259.
Melchiorre, E.B., Criss, R.E., Davisson, M.L., 1999b. Relationship between seismicity and subsurface fluids, central Coast Ranges, California. J. Geophys. Res. Solid Earth 104, 921–939.
Melchiorre, E.B., Criss, R.E., Rose, T.P., 2000. Oxygen and carbon isotope study of natural and synthetic azurite. Econ. Geol. 95, 621–628.
Melchiorre, E.B., Williams, P.A., 2001. Stable isotope characterization of the thermal profile and subsurface biological activity during oxidation of the Great Australia deposit, Cloncurry, Queensland, Australia. Econ. Geol. 96, 1685–1693.
Melchiorre, E.B., Enders, M.S., 2003. Stable isotope geochemistry of copper carbonates at the Northwest Extension Deposit, Morenci District, Arizona: implications for conditions of supergene oxidation and related mineralization. Econ. Geol. 98, 607–621.
Moldovanyi, E.P., Walter, L.M., Land, L.S., 1993. Strontium, boron, oxygen, and hydrogen isotope geochemistry of brines from basal strata of the Gulf Coast sedimentary basin, USA. Geochim. Cosmochim. Acta 57, 2083–2099.
Mügge, O., 1913. Uber die Minerale im Riickstand des roten Carnallits von Stassfurt und des schwarzen Carnallits von der Hildesia. Kali 7, 1–3.
Narbonne, G.M., 2005. The Ediacara biota: neoproterozoic origin of animals and their ecosystems. Annu. Rev. Earth Planet. Sci. 33, 421–442.
Popov, V., Sadykov, T., 1962. Authigenic tourmaline from rock salt deposits of Khodja-Mumyn. Dokl. Akad. Nauk USSR 145, 1121.
Rakovan, J., Waychunas, G., 1996. Luminescence in minerals. Mineral. Rec. 27, 7–19.
Reed, S.J.B., 2005. Electron Microprobe Analysis and Scanning Electron Microscopy in Geology. Cambridge University Press, Cambridge.
Reeder, R.J., Prosky, J.L., 1986. Compositional sector zoning in dolomite. J. Sediment. Petrol. 56, 237–247.
Rose, T.P., Davisson, M.L., Criss, R.E., 1996. Isotope hydrology of voluminous cold springs in fractured rock from an active volcanic region, northeastern California. J. Hydrol. 179, 207–236.
Rowland, J.C., Manga, M., Rose, T.P., 2008. The influence of poorly interconnected fault zone flow paths on spring geochemistry. Geofluids 8, 93–101.
Rutland, R.W.R., 1973. Tectonic evolution of the continental crust of Australia. In: Tarling, D.H., Runcorn, S.K. (Eds.), Implications of Continental Drift to the Earth Sciences. Academic Press, London, pp. 1011–1033.
Sawkins, F.J., 1976. Metal deposits related to intracontinental hotspot and rifting environments. J. Geol. 84, 653–671.
Seilacher, A., 1969. Fault-graded beds interpreted as seismites. Sedimentology 13, 155–159.
Sharp, Z., 2007. Principles of Stable Isotope Geochemistry. Pearson Education, Upper Saddle River, NJ.
Shi, G.R., Du, Y.S., Gong, Y.M., 2007. Soft-sediment deformation structures interpreted as seismite from the Middle Permian of the southern Sydney Basin, southeastern Australia. Aust. J. Earth Sci. 54, 861–874.
Spötl, C., Vennemann, T.W., 2003. Continuous-flow isotope ratio mass spectrometric of carbonate minerals. Rapid Commun. Mass Spectrom. 17, 1004–1006.
Sullivan, B., 1979. Letter from Europe. Mineral. Rec. 10, 121–124.
Thompson, B.J., Garrison, R.E., Moore, J.C., 2007. A reservoir-scale Miocene Injectite near Santa Cruz, California. In: Hurst, A., Cartwright, J. (Eds.), Sand Injectites: Implications for Hydrocarbon Exploration and Production, vol. 87. AAPG Memoir, pp. 151–162.
Walenta, K., Dunn, P.J., 1979. Ferridravite, a new mineral of the tourmaline group from Bolivia. Am. Mineral. 64, 945–948.
Walters, W.J., Claypool, G.E., Choquette, P.W., 1972. Reaction rates and $\delta^{18}O$ variation for the carbonate–phosphoric acid preparation methods. Geochim. Cosmochim. Acta 36, 129–140.
Warren, R.G., Shaw, R.D., 1995. Hermannsburg, Northern Territory 1:250,000 geological map series, explanatory notes. Northern Territory Geological Survey SF53-13.
Wilson, T.P., Long, D.T., 1993. Geochemistry and isotope chemistry of Ca–Na–Cl brines in Silurian strata, Michigan Basin, USA. Appl. Geochem. 8, 507–524.